



Thermal decomposition of tris(O-ethylthiocarbonato)-antimony(III)—a single-source precursor for antimony sulfide thin films

Jako S. Eensalu¹ · Kaia Tõnsuaadu² · Jasper Adamson³ · Ilona Oja Acik¹ · Malle Krunks¹

Received: 31 July 2020 / Accepted: 2 May 2021 / Published online: 20 June 2021
© The Author(s) 2021

Abstract

Thermal decomposition of tris(O-ethylthiocarbonato)-antimony(III) (**1**), a precursor for Sb₂S₃ thin films synthesized from an acidified aqueous solution of SbCl₃ and KS₂COCH₂CH₃, was monitored by simultaneous thermogravimetry, differential thermal analysis and evolved gas analysis via mass spectroscopy (TG/DTA-EGA-MS) measurements in dynamic Ar, and synthetic air atmospheres. **1** was identified by Fourier transform infrared spectroscopy (FTIR) and nuclear magnetic resonance (NMR) measurements, and quantified by NMR and elemental analysis. Solid intermediates and final decomposition products of **1** prepared in both atmospheres were determined by X-ray diffraction (XRD), Raman spectroscopy, and FTIR. **1** is a complex compound, where Sb is coordinated by three ethylthiocarbonate ligands via the S atoms. The thermal degradation of **1** in Ar consists of three mass loss steps, and four mass loss steps in synthetic air. The total mass losses are 100% at 800 °C in Ar, and 66.8% at 600 °C in synthetic air, where the final product is Sb₂O₄. **1** melts at 85 °C, and decomposes at 90–170 °C into mainly Sb₂S₃, as confirmed by Raman, and an impurity phase consisting mostly of CSO₂²⁻ ligands. The solid-phase mineralizes fully at ≈240 °C, which permits Sb₂S₃ to crystallize at around 250 °C in both atmospheres. The gaseous species evolved include CS₂, C₂H₅OH, CO, CO₂, COS, H₂O, SO₂, and minor quantities of C₂H₅SH, (C₂H₅)₂S, (C₂H₅)₂O, and (S₂COCH₂CH₃)₂. The thermal decomposition mechanism of **1** is described with chemical reactions based on EGA-MS and solid intermediate decomposition product analysis.

Keywords Antimony ethyl xanthate · Thermal degradation · Evolved gas analysis · Antimony sulfide · Decomposition mechanism

Introduction

Antimony sulfide (Sb₂S₃) is a material naturally suitable for application as the absorber layer in thin film solar cells. The crustal abundance and price of Sb (0.2 ppm; \$8.6 kg⁻¹), and S (340 ppm; \$0.05 kg⁻¹), which form the nontoxic Sb₂S₃, attest to its long-term economic viability as a strategic resource [1–3]. The anisotropic Sb₂S₃ has a bandgap of ≈1.7 eV, a high absorption coefficient of 1·10⁵ cm⁻¹ at 450 nm, a melting point of 550 °C, and is stable toward moisture, UV, and oxidation in air below 150 °C, being etched only by concentrated acid [4–7]. A bandgap of 1.7 eV makes Sb₂S₃ a prime candidate for application as the top cell absorber in tandem solar cells [8, 9], and as the thinner than 200 nm absorber in IR inactive semitransparent solar cells [10, 11].

Sb₂S₃ thin films have been fabricated from colloidal or metal–organic precursors by a number of solution-based

✉ Jako S. Eensalu
jako.eensalu@taltech.ee

✉ Malle Krunks
malle.krunks@taltech.ee

¹ Laboratory of Thin Film Chemical Technologies, Department of Materials and Environmental Technology, Tallinn University of Technology, Ehitajate tee 5, 19086 Tallinn, Estonia

² Laboratory of Inorganic Materials, Department of Materials and Environmental Technology, Tallinn University of Technology, Ehitajate tee 5, 19086 Tallinn, Estonia

³ Laboratory of Chemical Physics, National Institute of Chemical Physics and Biophysics, Akadeemia tee 23, 12618 Tallinn, Estonia

chemical methods, e.g., chemical bath (CBD) [12–14], atomic layer deposition (ALD) [15–17], spin-coating [18, 19], spray pyrolysis [11, 20–22], and by physical methods, e.g., thermal evaporation (TE) from inorganic targets [23], mainly for application as absorber in thin film solar cells. The highest power conversion efficiency achieved for planar Sb_2S_3 thin film solar cell is 6.6% by spin-coating a metal–organic complex of Sb, followed by annealing and Cs-doping [19], whereas the top power conversion efficiency of Sb_2S_3 solar cells is 7.5% [24]. Mass production of Sb_2S_3 solar cells with consistent power conversion efficiency requires use of simple and cost-effective methods, e.g., spray pyrolysis, as other methods are likely too expensive (vacuum, inert gas, specialty reagents for ALD, TE), too time consuming and waste-generating (CBD), or too small-scale (spin-coating) [25].

In order to fabricate Sb_2S_3 thin films from organometallic precursors, it is crucial to understand their decomposition mechanisms in oxidizing and inert atmosphere. Our laboratory has experience in analysis of formation of CuS, In_2S_3 , CuInS_2 , ZnS, and SnS thin films by employing TG/DTA-EGA for thiourea-based precursors to estimate the appropriate deposition conditions for spray pyrolysis in air [26–31]. The resulting thin films contained C and Cl impurities, except in case of Sb_2S_3 , where uniform thin films of Sb_2S_3 , free of C and Cl to detectable limits, were deposited at 210 °C by spray pyrolysis, wherein a liquid-phase reaction occurred due to a favorably low melting point of the precursors [22]. As lowering the deposition and annealing temperature of Sb_2S_3 thin films is critical for application as the ≈ 1.7 eV top absorber in tandem solar cells, the processing temperature must be decreased further. Moreover, lower processing temperature and shorter processing time would decrease the energy budget, ergo, the cost of producing Sb_2S_3 thin film-based solar cells and other devices, and increase the selection of usable substrates.

Metal xanthates, i.e., alkoxy- or aryldithiocarbonates, tend to decompose at low temperatures (100–250 °C) [32, 33], which is suitable to deposit metal chalcogenide thin films onto polymer substrates for flexible applications, and to fabricate the top cell for tandem solar cells. However, the decomposition mechanism and temperature of each xanthate depend significantly on the combination of cation [34], and ligand [33], meaning that TG/DTA-EGA could be of use. Xanthates, e.g., potassium ethyl xanthate ($\text{KS}_2\text{COCH}_2\text{CH}_3$, KEX) were discovered by W. C. Zeise in 1822 [4]. Since then, xanthates and related organometallic compounds are being used in ore flotation, in organic chemistry, in analytical chemistry, in biochemistry, in coordination chemistry, and in materials science to fabricate metal chalcogenide powders and layers, e.g., ZnS, NiS, Fe_2S_3 , Cu_2S , PbS, As_2S_3 , Sb_2S_3 , Bi_2S_3 , and lead-free perovskites [4, 32, 34–44]. Antimony ethyl xanthate (SbEX) has risen to prominence in the last

decade as a single-source precursor to fabricate Sb_2S_3 powders for various applications, or to make porous layers for use as the absorber in solar cells by solution-based chemical methods, e.g., solvothermal, or spin-coating coupled with post-deposition annealing at 160–240 °C [33, 39, 45].

A comprehensive thermal decomposition study of SbEX, where TG/DTA is coupled with evolved gas analysis and intermediate solid decomposition product analysis, has not been published. Sporadic studies of TG curves of SbEX have been published with contradictory and vague statements regarding the temperature required to produce phase pure Sb_2S_3 [32, 33, 39, 45]. Therefore, a comparative study of the TG/DTA-EGA-MS of SbEX in inert and oxidizing atmosphere is required to determine its suitability for depositing phase pure Sb_2S_3 thin films for application in semitransparent, bifacial, and as the top cell absorber in tandem solar cells, in addition to other semiconductor applications.

Aiming to determine the viability of SbEX as a single-source precursor for depositing Sb_2S_3 thin films by ultrasonic spray pyrolysis, we investigate the thermal decomposition of SbEX in inert and synthetic air atmosphere in this study by TG/DTA-EGA-MS coupled with analysis of the solid intermediate decomposition products of SbEX, and describe the mechanism of thermal decomposition of SbEX.

Experimental

Synthesis

Potassium ethyldithiocarbonate (potassium ethyl xanthate, KEX) (> 97 mass%, Acros) and antimony(III)chloride (SbCl_3) (99 mass%, Sigma-Aldrich), deionized water ($18.2 \text{ M}\Omega\text{cm}^{-1}$), and HCl (≥ 37 vol%, Sigma-Aldrich) were employed for the synthesis of the precursor for thermal analysis. All chemicals were used as-bought without further purification. The precursor for thermal analysis was synthesized according to the literature [40], with some modifications.

The precursor was synthesized at room temperature by pouring 375 mM of KEX to 200 mL of 125 mM SbCl_3 , acidified beforehand with HCl to retain SbCl_3 , while stirring. A bright yellow substance started precipitating immediately upon mixing. The solution was stirred for 60 min. The precipitate was rinsed with deionized water, diethyl ether (99.5 vol%, Sigma-Aldrich), and acetone (99.8 vol%, Merck), then recrystallized from acetone and rinsed with water at 83% yield. This product, named **1** going forward, was used for further analysis.

Elemental analysis

The elemental composition of **1** was analyzed by energy-dispersive X-ray spectroscopy (EDX) on a Zeiss Ultra 55 FEG HR-SEM setup equipped with a Bruker ESPRIT 1.8 system. The atomic ratio of S/Sb was found to be 5.7 ± 0.1 , which is 93–97% of the expected stoichiometric atomic ratio of S to Sb of 6.0 in SbEX.

Nuclear magnetic resonance analysis

The nuclear magnetic resonance (NMR) analysis was carried out on a 800 MHz Bruker Avance III setup connected with a 18.8 T magnet/ 54 mm heat opening diameter at 25 °C. Samples of **1** were weighed, and dissolved in CDCl_3 (99.8 vol%, Eurisotop) for 1D qualitative ^1H , 1D quantitative ^{13}C , 2D homonuclear correlation spectroscopy (COSY), heteronuclear single-quantum correlation spectroscopy (HSQC), and heteronuclear multiple-bond correlation spectroscopy (HMBC) NMR. For 1D quantitative ^1H analysis, **1** and 2-Propanol (99.9 vol%, Sigma-Aldrich) were weighed in a fixed molar ratio on a microbalance after antistatic screening, and co-dissolved in CD_3OD (MeOD, 99.8 vol%, Eurisotop). Chemical shifts in ppm were calibrated relative to CDCl_3 and MeOD. The residual mass of **1** in the weighing tray was subtracted before quantification. NMR data were analyzed, and figures were generated using Mestrelab MNova software.

Vibrational analysis

The FTIR spectra of KEX and **1** were measured on a FTIR setup (Perkin Elmer GX 2000), 400–4000 cm^{-1} , 4 cm^{-1} resolution, 32 scans, by the KBr pellet method, using the FTIR spectrum of the KBr pellet as background. 1.0 mass% of sample per 200 mg of KBr, pre-dried in air at 150 °C for 1 h, was pressed into a 13 mm-diameter pellet after grinding the mixture with a corundum pestle and mortar.

The FTIR spectra of **1**, and its intermediate decomposition products prepared at 115 °C, and at 160 °C in flowing N_2 , and air were measured on a Bruker Alpha FTIR setup, equipped with a diamond anvil in absorbance mode, 24 scans, resolution 4 cm^{-1} .

In addition, Raman spectra of **1** and its intermediate solid decomposition products were measured on a micro-Raman setup (Horiba LabRam 800, 15 μW μm^{-2} , 532 nm He–Ne, \varnothing 5 μm), calibrated with 546.1 nm Hg line. Raman data were analyzed with Fityk software [46]. FTIR and Raman figures were generated with OriginLab software.

Thermal analysis

The simultaneous TG/DTA/EGA-MS measurement of **1** was performed in a Setaram LabSys EVO apparatus, using a heating rate of 10 °C min^{-1} , purge gas (Ar or 80% Ar, 20% O_2 –synthetic air) with a flow rate of 60 mL min^{-1} , sample mass 14.2 mg (in Ar), and 13.5 mg (in synthetic air) in open Al_2O_3 crucible. The gaseous species were guided into a ThermoStar GSD320 quadrupole mass spectrometer through a heated capillary tube kept at 180 °C. Data were collected in multiple ion detection mode (MID) monitoring 21 channels between $m/z = 1$ –89. Collection time was 1 s for each channel. EGA-MS figures were generated with OriginLab software.

The evolved gases were identified based on their MS reference spectra available in the public domain spectral library of NIST [47]. Reaction schemes were generated with ACD ChemSketch freeware.

Intermediate decomposition product preparation

Intermediate decomposition products of **1** were prepared in inert atmosphere in laboratory test as follows: after purging the quartz tube inside the two-zone tube furnace to $1 \cdot 10^{-3}$ mbar at room temperature, 99.999% N_2 flow of 60 mL min^{-1} , and heating rate of 10 °C min^{-1} were used, while retaining the ceramic crucible at 170 °C, 270 °C, 400 °C, or 730 °C for 10 min before cooling in ambient to ≈ 40 °C and withdrawing. Intermediate decomposition products of **1** in air were prepared in laboratory test at 170 °C, 270 °C, and 480 °C by inserting **1** into a preheated muffle furnace, and retaining the specified temperature in the crucible for 10 min before withdrawing. At 600 °C, the residue from TG/DTA in synthetic air was used.

For FTIR analysis of the products of the first decomposition step, intermediate decomposition products of **1** were prepared in inert atmosphere in the same two-zone tube furnace as follows: after purging to $1 \cdot 10^{-3}$ mbar at room temperature, 99.999% N_2 flow of 30 mL min^{-1} , and heating rate of 5 °C min^{-1} were used, while retaining the crucible at 115 °C, or 160 °C for 3 min before cooling in ambient to ≈ 40 °C and withdrawing. For FTIR analysis of the first decomposition step, intermediate decomposition products of **1** in air were prepared as follows: **1** was inserted into a preheated muffle furnace and heated in a semi-closed crucible, to prevent the solid from surging out, at the specified temperature for 3 min before withdrawal, and immediately cooled in a cold water bath to room temperature.

Structural analysis

The phase composition of **1**, its intermediate and final decomposition products were analyzed with a powder XRD (Rigaku Ultima IV, Si strip detector D/teX Ultra), Cu K α_1 λ 1.5406 Å, θ -2 θ mode, 5°min⁻¹, step 0.02°, 40 kV, 40 mA. XRD data were analyzed using Rigaku PDXL 2 software. Figures were generated with OriginLab software.

Results and discussion

Identification of **1**

The FTIR spectra of potassium ethyl xanthate (KS₂COC₂H₅ – KEX) and antimony ethyl xanthate (Sb(S₂COC₂H₅)₃ – SbEX) have been published before, being only presented in this study to identify and demonstrate the purity of KEX and **1**. FTIR spectra of KEX and **1**, as measured by the KBr technique, are shown in Fig. 1. The list of possible assignments of FTIR bands of KEX and **1**, based on the literature [36, 38, 41–43, 48, 49], is presented in Table S1 in the electronic Supporting File.

According to FTIR, the spectra of KEX and **1** were similar, although bands had shifted in the range of 1300 cm⁻¹–1000 cm⁻¹ in **1** vs KEX, showing that the complex with Sb seems to have formed. The C=S stretching modes shifted from 1006 cm⁻¹ and 1050 cm⁻¹ in KEX to 1001 cm⁻¹, and 1024 cm⁻¹ in **1**, indicating the formation of longer C-S bonds as a result of the stronger electron pull toward Sb in the Sb-S bond than in the K-S bond due to Sb being more electronegative than K. The symmetric C–O–C stretching (1103 cm⁻¹, 1118 cm⁻¹) in KEX, shifted to 1112 cm⁻¹, and 1135 cm⁻¹ in **1**. The asymmetric C–O–C stretching (1158 cm⁻¹, 1173 cm⁻¹) in KEX, merged into a

strong band at 1230 cm⁻¹ in **1**. C–O–C stretching modes shifting to higher wavenumbers likely points to a shortening of C–O–C bonds in the ligand. Weaker bands appearing at 3000–2870 cm⁻¹, 1468 cm⁻¹, 1448 cm⁻¹, 1075 cm⁻¹ and 813 cm⁻¹ attributed to CH₃ and CH₂ stretching and bending modes did not shift considerably, revealing that the interaction between the ethyl group and the cation (K, Sb) is weak, as expected. Therefore, the ethyl group is the farthest, and the CS₂ group is probably the closest to Sb, connected to each other by the C–O–C bridge. The wide band positioned at 3650–3300 cm⁻¹ in both KEX and **1** is attributed to adsorbed H₂O.

The Raman spectrum of **1** is shown in Fig. S1. So far, the Raman spectrum of SbEX is unindexed, though 35 Raman active optical modes in the range of 50–3000 cm⁻¹ were observed in the Raman spectrum of **1**. The most intense Raman bands of **1** are centered at 91, 167, 232, 339, 406, 439, 665, 845, 998, and 1029 cm⁻¹. Raman band centers of **1**, with possible assignments from compounds similar to SbEX [43, 48, 50], are listed in Table S2. Raman bands attributed to only **1** were found above the limit of detection.

The crystal structure of SbEX is rhombohedral, space group R $\bar{3}$, $a = 10.13$ Å, $\alpha = 103^\circ 30'$, six units in the unit cell, and each Sb atom is known to be surrounded by three S atoms at 2.52 Å, and another three at 3.00 Å, which altogether form a distorted octahedron, extending into the planar S₂C–O group [51, 52]. The XRD pattern of rhombohedral SbEX is available in the CSD database under SBXANT, and the XRD pattern of **1** is presented only to confirm its identity as SbEX (Fig. S2, numeric data in Table S3). According to XRD, additional phases above the limit of detection were not found in **1**.

The 1D NMR analysis results are presented in Table 1. Minor traces of acetone and ethanol were found in **1**. Evidently, the acquired ¹H and ¹³C NMR data correspond to

Fig. 1 FTIR spectra of potassium ethyl xanthate (KEX) and **1** recorded with 4 cm⁻¹ resolution in KBr pellet

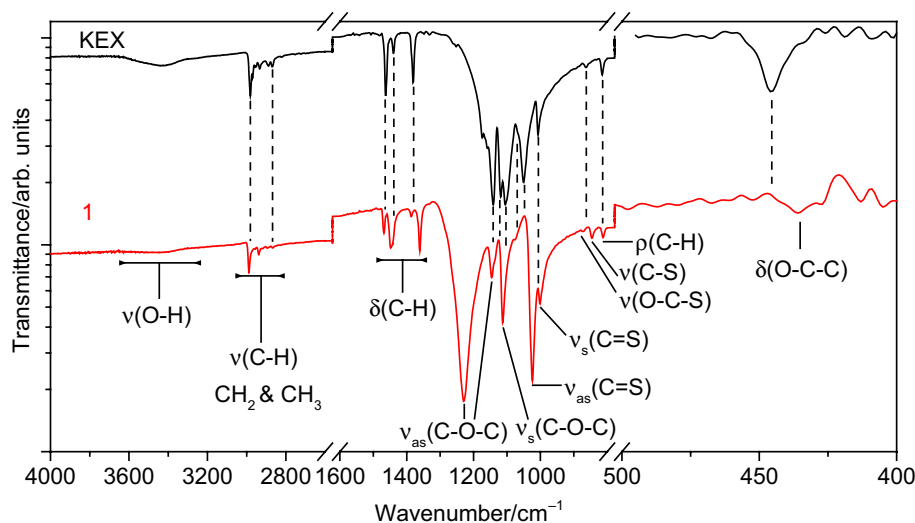


Table 1 ^1H and ^{13}C spectral data of **1** in comparison to the literature [33, 53]

Compound	^1H / ppm		Ref	^{13}C / ppm		Ref	Integral of ^1H		Functional group
	Found in 1	Literature		Found in 1	Literature		1	2-PrOH	
CDCl_3	7.26, s	7.26	[53]	77.16	77.16	[53]	–	–	CHCl_3
CH_3COCH_3	2.17, s	2.17	[53]	–	30.92	[53]	–	0.01	$-\text{CH}_3$
2-PrOH	1.20, d	1.22	[53]	25.48	25.14	[53]	–	6.26	$-\text{CH}_3$
	4.01, sept	4.04	[53]	64.53	64.50	[53]	–	1.00	$-\text{CH}-$
1	1.47, t	1.40	[33]	14.00	12.40	[33]	3.00	4.18	$-\text{CH}_3$
	4.64, q	4.55	[33]	72.17	71.00	[33]	2.00	2.15 ^a	$-\text{CH}_2-$
	–	–	–	222.60	221.40	[33]	–	–	$-\text{O}-\text{C}-\text{S}_2$

^aThe CH_2 functional group was used to calculate the purity of **1** with respect to the known amount of 2-PrOH. There was overlap between the signals for the CH_3 functional group of 2-PrOH and the CH_3 functional group of **1**, which prevented accurate integration of these proton peaks

Table 2 COSY, HSQC and HMBC spectral data of **1**

Method	^1H / ppm		^{13}C / ppm	Functional groups ^a
COSY	1.43	4.65	–	$-\text{CH}_2-\text{CH}_3$
	4.60	1.48	–	
HSQC	1.46		14.04	$-\text{CH}_3$
	4.64		72.16	$-\text{CH}_2-$
HMBC	4.64		14.04	$-\text{CH}_2-\text{CH}_3$
	1.46		72.16	$-\text{CH}_2-\text{CH}_3$
	4.64		222.60	$\text{S}_2-\text{C}-\text{O}-\text{CH}_2-$

^aHMBC correlated nuclei are in bold

relevant values in the literature [33, 53], thereby complementing the FTIR data in identification of **1**.

According to quantitative ^1H of CH_3 , the analyte contained the equivalent of 95 mol% of (EX)₃ versus 2-PrOH (Table 1). The remaining 5 mol% of **1** precipitated in the NMR test tube. According to XRD, the red precipitate was amorphous, as no reflections were observed. The Raman spectrum of the precipitate contained a single broad band, stretching from 200–360 cm^{-1} , and centered at 290 cm^{-1} , characteristic of amorphous Sb_2S_3 [21, 22]. Thus, the results of quantitative NMR, XRD, and Raman support the observations made in EDX analysis of **1** regarding its slight deficiency of sulfur (S/Sb of 1.42) vs stoichiometric composition of S/Sb of 1.50. Indeed, it is known that SbEX can change from light yellow to dark yellow, then to orange by decomposing over time to amorphous Sb_2S_3 [36].

Based on the liquid NMR COSY analysis (Table 2), **1** contains mutually J-bonded CH_3 and CH_2 groups. HSQC analysis revealed that the two observed peaks at (^1H 1.46; ^{13}C 14.04) and (^1H 4.64; ^{13}C 72.16) correlate with one another, proving that the CH_3 and CH_2 functional groups are directly bonded in **1**. According to HMBC analysis, three cross-peaks appeared (Table 2; Fig. S3). Thus, the CH_2 functional group is bonded to both the CH_3 , and the OCS_2 functional group and the sequence of functional groups in **1**

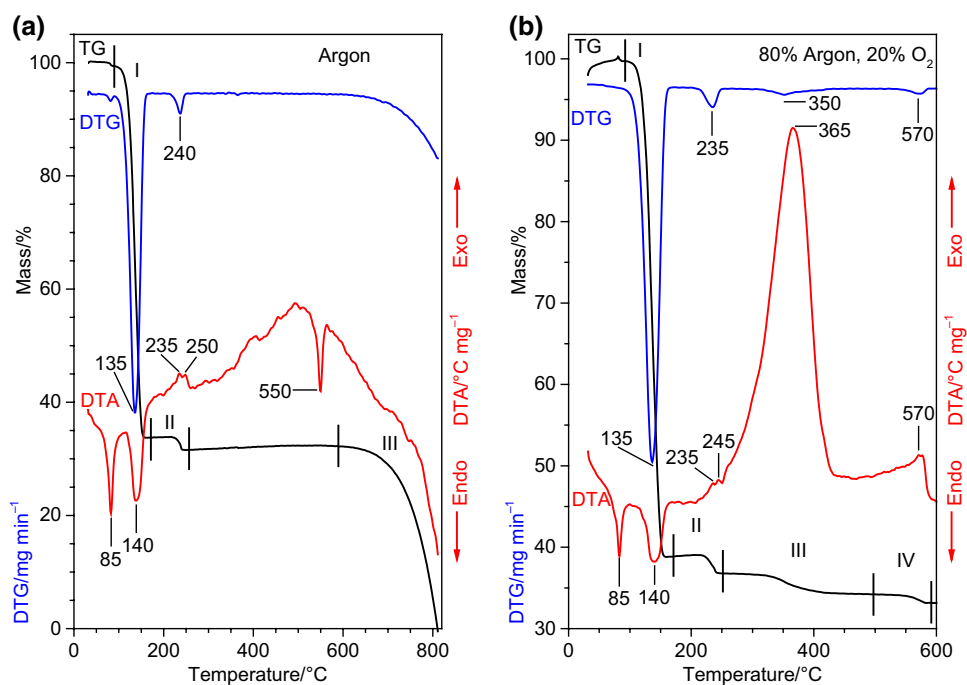
can be derived as $\text{CH}_3-\text{CH}_2-\text{O}-\text{CS}_2-$. The quantitative 1D ^1H NMR experiment showed that the molar ratio of CH_3 functional groups in **1** to 2-PrOH is 1.42 (expected 1.50, *i.e.*, 3/2). As ≈ 5 mol% of **1** is Sb_2S_3 , then the molar ratio of CH_3 in the EX ligand to Sb^{3+} is close to the expected stoichiometric value of 3.

In summary, FTIR showed that the vibrational modes of **1** correspond to only SbEX, and the main bands had shifted in comparison to KEX, indicating the formation of a complex with a more electronegative metal. XRD showed that only rhombohedral SbEX was detected in **1**. Raman showed that bands attributed to only **1** were detected. Further investigation by NMR showed that there are approximately three ligands per molecule of **1** with the structure of $-\text{S}_2\text{COCH}_2\text{CH}_3$, *i.e.*, the EX ligand. According to quantitative ^1H NMR, **1** contains approximately 95 mol% of SbEX. The slight deficiency of S was also observed by EDX (95 ± 2 mol% of theoretical value). The remaining 5 mol% was identified as amorphous Sb_2S_3 by Raman. Therefore, **1** has been identified as 95 mol% $\text{Sb}(\text{S}_2\text{COCH}_2\text{CH}_3)_3 - \text{SbEX}$, and 5 mol% of amorphous Sb_2S_3 .

Thermal analysis

According to TG curves of **1** (Fig. 2), the thermal decomposition occurred in three mass loss steps in argon in the range of 90–800 $^\circ\text{C}$, whereas in synthetic air, four mass loss steps were observed in the range of 90–590 $^\circ\text{C}$. The endothermic step at 85 $^\circ\text{C}$ in both atmospheres is the melting point of **1**, because in laboratory test, a melting point of **1** of 77 ± 1 $^\circ\text{C}$ was measured on slow heating in air (*cf.* 75 $^\circ\text{C}$ in [32], 68–70 $^\circ\text{C}$ in [33]), wherein a viscous adhesive clear yellow liquid formed. The first mass loss step was endothermic in both atmospheres, as DTA peaked at 140 $^\circ\text{C}$, preceding the DTG maximum at 135 $^\circ\text{C}$. Similarly, in both atmospheres, two consecutive exothermic effects occurred in the second mass loss step at 235 $^\circ\text{C}$ and 250 $^\circ\text{C}$ in argon, and 235 $^\circ\text{C}$ and 245 $^\circ\text{C}$ in synthetic air, together with a DTG maximum

Fig. 2 TG, DTG, and DTA curves of **1** in **a** argon, flow 60 mL min⁻¹, heating rate 10 °C min⁻¹, initial mass 11.6 mg, and **b** synthetic air, flow 60 mL min⁻¹, heating rate 10 °C min⁻¹, initial mass 13.9 mg, as measured in situ by the online coupled TG/DTA-MS system



positioned at 240 °C in argon, and 235 °C in synthetic air, respectively.

Mass was constant in argon between 250 and 590 °C, although a sharp endothermic effect occurred at 550 °C. A broad endothermic effect occurred throughout the third mass loss step in argon beginning at 600 °C. An intense exothermic effect appeared in the third mass loss step in synthetic air, peaking at 365 °C, trailing the DTG peak at 350 °C. A weaker exothermic effect occurred in the fourth mass loss

step in synthetic air at 570 °C simultaneously with the DTG peak at 570 °C.

The first mass loss step in both atmospheres was in the range of 90–170 °C with mass losses of 66.3% in argon, and 61.1% in synthetic air. The second mass loss step was in the range of 170 °C–255 °C in argon, and 170 °C–250 °C in synthetic air, with mass loss of 2.1% in both cases. The third mass loss step started in argon at 590 °C, proceeding until 810 °C, where all of the remaining mass was lost. The mass

Table 3 Decomposition steps, mass losses, temperatures of DTA and DTG peaks, evolved gases, and detected crystalline phases of **1**. TG/DTA-MS data recorded using a heating rate of 10 °C min⁻¹ in argon,

and synthetic air atmosphere with open Al₂O₃ crucible on a Setaram LabSys EVO instrument

Atmosphere	Step	Temperature range/°C	Mass loss at the end of the decomposition step /%	DTA peak temp./°C	DTG max temp./°C	Evolved gases from MS ^a	Crystalline phases at the end of the decomposition step (XRD data), ICDD PDF No
Ar	1	90–170	66.3	140 endo	135	CS₂, EtOH, CO, CO₂, COS	None
	2	170–255	68.4	235 exo, 250 exo	240		
	3	590–800	100	–	–	–	Sb ₂ S ₃ , Sb (05–0562) at 730 °C
	Final	800 °C	100	–	–	–	no solid residue
Ar + O ₂	1	90–170	61.1	140 endo	135	CS₂, EtOH, CO, CO₂, COS	None
	2	170–250	63.2	235 exo, 245 exo	235		
	3	250–495	65.8	365 exo	350	SO ₂	Sb ₂ O ₄ (cervantite, 01–074-8714)
	4	495–590	66.8	570 exo	570	SO ₂	Sb ₂ O ₄ (600 °C)
	Final	600 °C	66.8	–	–	–	Sb ₂ O ₄

^aMajor gases in bold

loss of **1** in argon above 590 °C is the result of incongruent evaporation of liquid Sb_2S_3 per the Sb-S phase diagram [5, 7, 54], as the product collected at 730 °C consisted of crystalline Sb_2S_3 and metallic Sb according to XRD (Table 3).

In synthetic air, the third mass loss step was in the range of 250–495 °C with mass loss of 2.6%. The fourth mass loss step in synthetic air was in the range of 495–590 °C with mass loss of 1.0%. Final mass loss was 100% in argon at 800 °C, and 66.8% in synthetic air at 600 °C. The theoretical mass loss in argon at 600 °C is 65.0% (experimental 68.3%), assuming pure Sb_2S_3 phase. The theoretical mass loss in air is 68.3%, as the final product in synthetic air was Sb_2O_4 . The final mass loss of **1** in synthetic air was lower than calculated due to presence of Sb_2S_3 in **1**.

Evolved gas analysis in argon and synthetic air atmosphere by online EGA-MS

The evolution curves of gases as ion currents of characteristic mass fragments of the identified gaseous species vs temperature evolved from **1** in argon, and in synthetic air in comparison, as recorded by online EGA-MS, are shown in Fig. 3. Peak centers and assignments of all measured EGA-MS channels are listed in Table S4.

According to EGA-MS in argon, the evolution of gases started at 50 °C with the evolution of adsorbed moisture as water (H_2O) with characteristic ion fragment of m/z 18, peaking at 82 °C. Evolution of water below 100 °C was not detected in synthetic air likely because the sample was purged for an extended period of time vs the sample in argon before commencing the EGA-MS run.

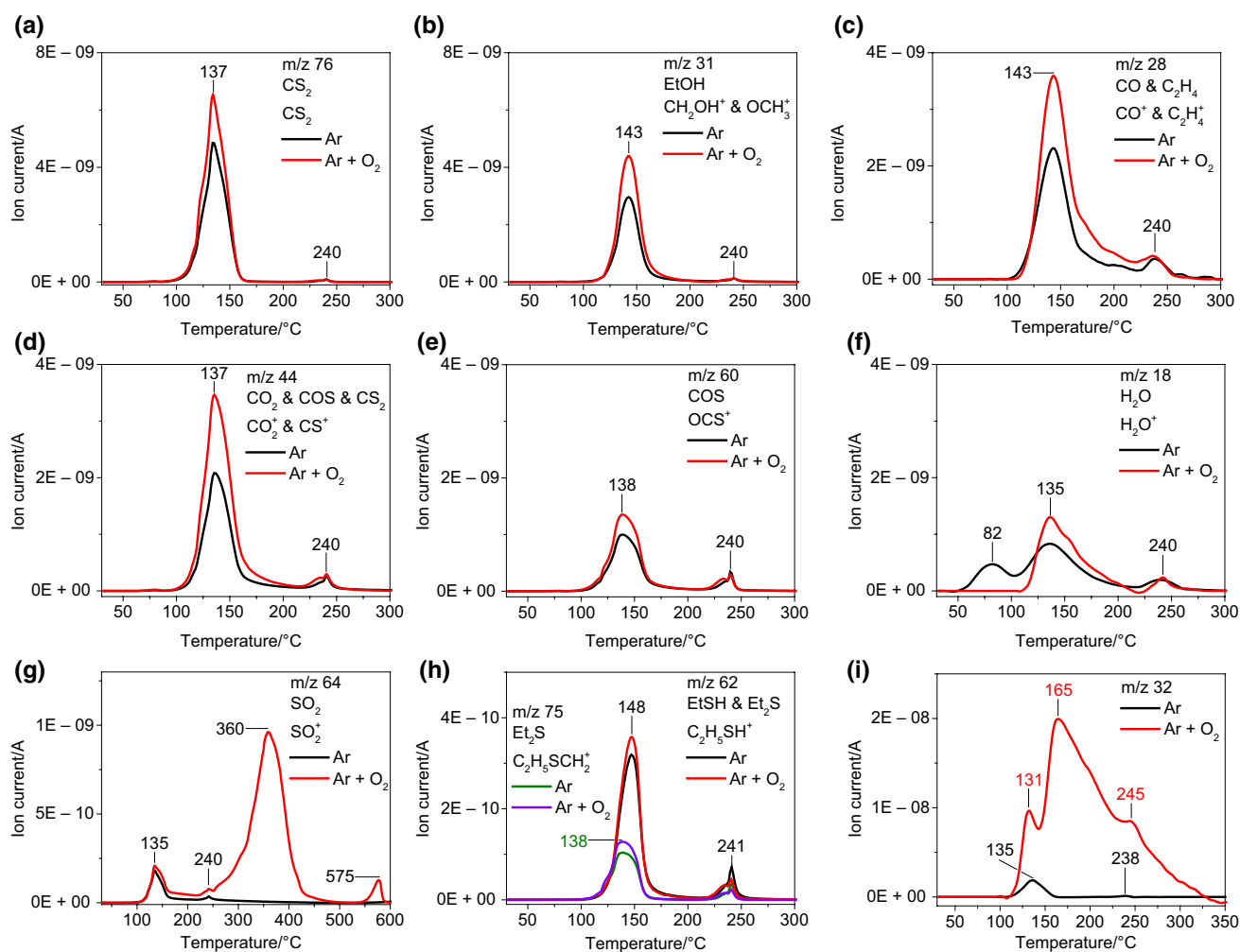


Fig. 3 Gas evolution profiles of CS_2 **a**, EtOH **b**, CO and C_2H_2 **c**, CO_2 , CS_2 , and COS **d**, COS **e**, H_2O **f**, SO_2 **g**, EtSH and Et_2S **h**, and unknown m/z 32 **i**, represented by their characteristic mass spectroscopic ion fragments, from **1** in argon (in black or green), flow

60 mL min^{-1} , heating rate 10°min^{-1} , initial mass 11.6 mg, and in synthetic air (in red or violet), flow 60 mL min^{-1} , heating rate 10°min^{-1} , initial mass 13.9 mg, as measured by in situ online coupled TG/DTA-EGA-MS system. (Color figure online)

The first decomposition step (90–170 °C) began similarly in argon and synthetic air with the evolution of several gases: carbon disulfide (CS₂, *m/z* 76, Fig. 3a), ethanol (EtOH, *m/z* 31, Fig. 3b), carbon monoxide (CO, *m/z* 28, Fig. 3c; possibly partially attributable to C₂H₄), carbon dioxide (CO₂, *m/z* 44, Fig. 3d; partially attributable to CS⁺ from CS₂ and COS), carbonyl sulfide (COS, *m/z* 60, Fig. 3e), water (*m/z* 18, Fig. 3f), and sulfur dioxide (SO₂, *m/z* 64, Fig. 3g). Substantial evolution of gaseous fragments corresponding to the methyl group (CH₃, *m/z* 15, Fig. S4a), and the ethyl or formyl group (C₂H₅ or CHO, *m/z* 29, Fig. S4b) was also detected. Evolution of some minor gases was also detected, *e.g.*, ethanethiol (EtSH, *m/z* 62, Fig. 3h), diethyl sulfide (Et₂S, *m/z* 75, Fig. 3h), diethyl ether (Et₂O, *m/z* 74, Fig. S4c) and dixanthogen ((EX)₂, *m/z* 89, Fig. S4d).

In argon, the evolution curve of the tentatively unassigned *m/z* 32 corresponded to CS₂, COS, and SO₂, with a maximum at 135 °C. Thus, in argon, *m/z* 32 is attributed to the S⁺ fragment of CS₂, COS, and SO₂, and possibly to molecular MeOH. The evolution curve of *m/z* 32 in synthetic air is a conundrum, because after 131 °C the curve is unlike any of the monitored *m/z* channels, its intensity looming over other gases by an order of magnitude without mass loss nor any DTA effects. This strange phenomenon was observed in experiments run in synthetic air with Al₂O₃ and Pt crucible (not shown), where the shape and intensity of the evolution curve were similarly anomalous. In synthetic air, *m/z* 32 could correspond to S⁺ (COS, CS₂, H₂S, S₈), or MeOH, but comparison to other *m/z* curves disproved this possibility. Therefore, *m/z* 32 in synthetic air remained unresolved in this study.

The second decomposition step (170–255 °C in argon, 170–250 °C in synthetic air) proceeded with the evolution of CS₂, EtOH, CO, CO₂, COS, H₂O, SO₂, EtSH, Et₂S, Et₂O, and (EX)₂ in a proportionally smaller quantity, reflecting the ≈30 times smaller mass loss in the second decomposition step compared to the first (2.1% vs. 66.3% in argon; 2.1% vs. 61.1% in synthetic air). In the second decomposition step in argon, and synthetic air the evolution curves of gases were asymmetric, tailing toward lower temperatures, peaking at 240 °C. The asymmetric evolution curve in EGA-MS supports the TG/DTA results in that two consecutive exothermic processes occur in the second decomposition step, peaking at 235 °C and 250 °C in argon, and at 235 °C and 245 °C in synthetic air (Fig. 2). The evolution of most gaseous species ceased by the end of the second decomposition step at ≈270 °C, indicating complete decomposition of organic material. In argon, no evolution of gases was detected beyond 270 °C, whereas in synthetic air, only SO₂ and *m/z* 32 continued to evolve.

In the third decomposition step in synthetic air (250–495 °C), SO₂ evolved in a significantly larger amount

than in the first and second step, peaking at 360 °C. In the fourth decomposition step in synthetic air (495–590 °C), SO₂ evolved from 530 to 590 °C, peaking at 575 °C. The evolution curve of SO₂ in synthetic air closely resembles the DTA curve (Fig. 2b), and follows the DTG peak positions in the temperature range of 200–600 °C, indicating that the exothermic DTA effects in that temperature range in synthetic air are directly related to the evolution of SO₂.

Discussion of thermal analysis results

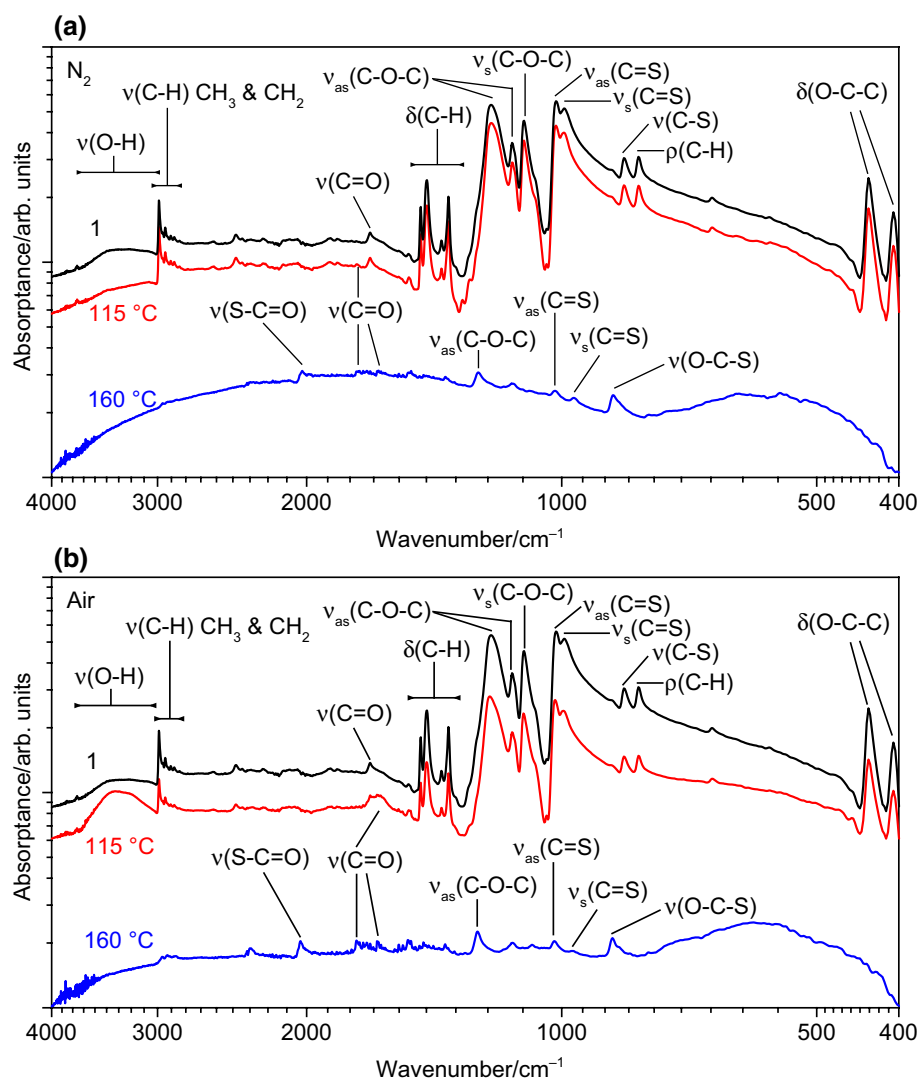
To establish the basis for describing the decomposition mechanism of **1**, laboratory tests were made to investigate the phase composition of the *solid* intermediate decomposition products of **1** at various temperatures in inert and air atmosphere. These intermediate decomposition products of **1** were characterized by FTIR, XRD, and Raman to determine the phase composition at various stages of the decomposition process.

The slight difference in FTIR spectra of some band positions of **1** in respect to measurements by KBr method is attributed to differences in instrument setup and measurement mode (Fig. 1 vs. Fig. 4). Tentative FTIR assignments in the following discussion are based on the literature [36, 38, 41–43, 48–50, 55–57]. According to FTIR, the vibrational modes of the intermediate decomposition product prepared at 115 °C in N₂ are nearly identical to those of **1** (Fig. 4a).

By 160 °C, the FTIR spectrum has changed significantly, as bands attributed to CH₃ and CH₂ stretching (2800–3000 cm⁻¹), scissoring (1386 cm⁻¹, 1443 cm⁻¹, 1468 cm⁻¹), twisting (1075 cm⁻¹), and rocking (813 cm⁻¹) modes have disappeared, indicating that the ethyl group (CH₃CH₂-) has been cleaved, and has exited into the gas phase. Furthermore, the O–C–C scissoring (407 cm⁻¹, 436 cm⁻¹) of the ethyl group has disappeared, in correlation with EGA-MS results, where evolution of EtOH peaked at 143 °C, and ended by 160–165 °C (Fig. 3b). Adsorbed water has evolved by 160 °C in N₂, because the broad band (O–H stretching, 3000–3700 cm⁻¹) is not present in the spectrum of the solid intermediate (Fig. 4a). Moreover, by 160 °C in N₂, bands have shifted from 995 cm⁻¹ to 967 cm⁻¹ (C=S symmetric stretching; bond elongation), from 1230 cm⁻¹ to 1254 cm⁻¹ (C–O–C asymmetric stretching; bond shortening), and from 1682 cm⁻¹ to 1643 cm⁻¹ (conjugated C=O stretching; bond elongation) (Fig. 4a). The shift in band positions and new bands at 870 cm⁻¹ (O–C–S stretching), and 2021 cm⁻¹ (S–C=O stretching) likely indicates the formation of a monothiocarbonate ligand (CSO₂²⁻).

The FTIR spectrum of the solid intermediate prepared at 115 °C in air is similar to the spectra of **1** and the solid intermediate prepared at 115 °C in N₂, although some features differ: a C=O stretching band at 1643 cm⁻¹ in air vs 1742 cm⁻¹ in N₂, and a more intense band between

Fig. 4 FTIR spectra of **1** and its intermediate decomposition products prepared in laboratory tests in N₂ **a**, and in air **b** in the first decomposition step at 115 °C and 160 °C, as measured with diamond anvil in reflectance mode at resolution of 4 cm⁻¹, 24 scans

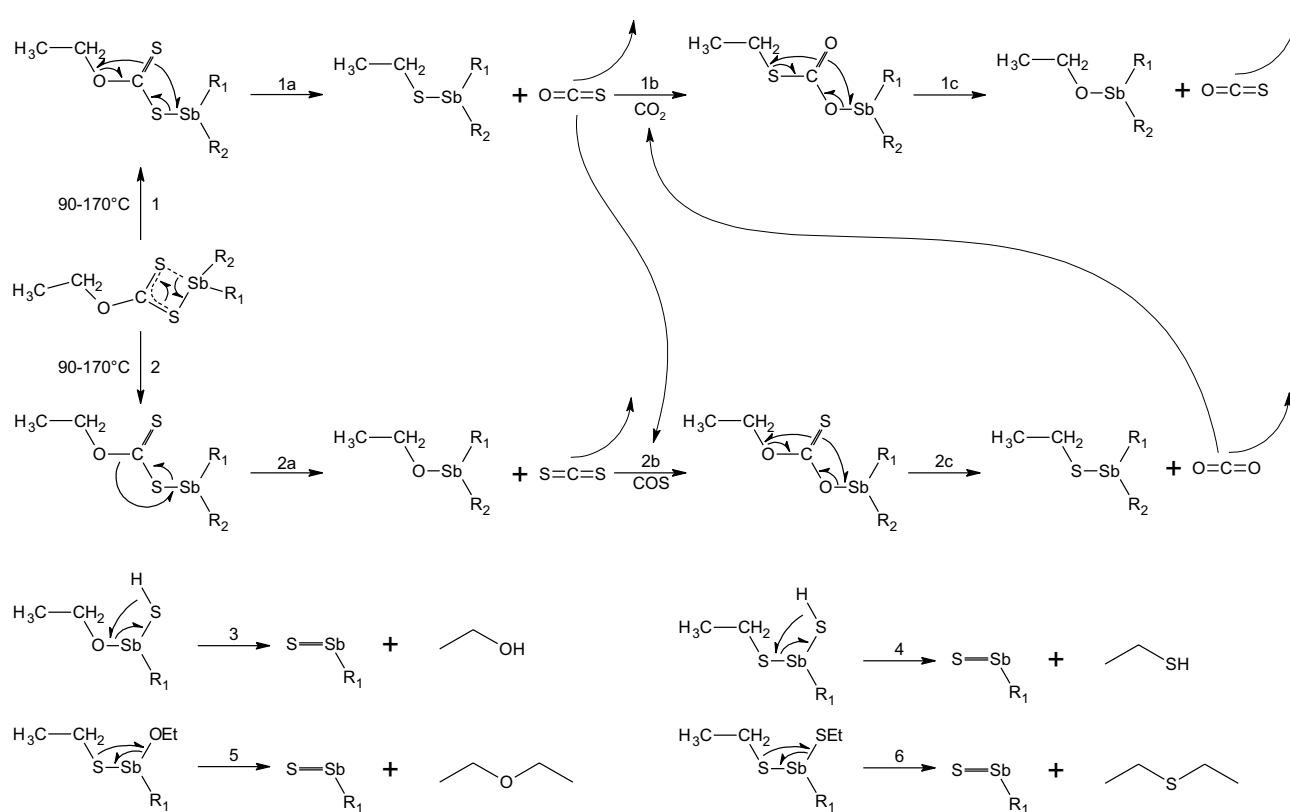


3000–3700 cm⁻¹ than in **1** (O–H stretching), showing that free water has formed during the decomposition of **1** due to air oxidation of the ethyl group. The FTIR spectrum of the solid intermediate prepared at 160 °C in air is similar to the spectrum of the residue prepared at 160 °C in N₂, except a weak residual of the ethyl group at 2800–3000 cm⁻¹ (CH₃, CH₂ stretching) possibly due to insufficient time for decomposition of **1** in laboratory test. In summary, the intermediate decomposition products prepared at 160 °C in N₂, and in air appear to contain one or more ligands composed of C=O, C–S, O=C–S, O–C–S, and possibly C–O–C fragments, with traces of ethyl group.

The main gases CS₂, EtOH, CO, CO₂, COS, and H₂O co-evolve in the first decomposition step, thus, the decomposition of SbEX cannot proceed merely by direct cleavage of the EX ligand, and must proceed through one or more parallel reactions. As SbEX is liquid before and during the decomposition, liquid-phase radical and ionic reactions that are common for xanthate reactions should occur [35, 37].

COS, CS₂ and EtOH likely form via competing reactions, where one Sb–S coordination bond is broken, followed by intramolecular rearrangement of bonds between the alkoxy and dithiocarbonyl group (Scheme 1, reaction 1 and reaction 2). With rotation of the dithiocarbonyl group, followed by cleavage of COS that evolves as a gas, Sb(R₁)(R₂)SCH₂CH₃ is produced (Scheme 1, reaction 1a). Without rotation of the dithiocarbonyl group, CS₂ is cleaved, evolving as a gas, and Sb(R₁)(R₂)OCH₂CH₃ (Scheme 1, reaction 2a) is produced. Reaction 2 and reaction 2a in Scheme 1 is most likely the main reaction, as this sequence is the most straightforward and credible source of CS₂—the main evolved gas. Reaction 2a is likely thermodynamically preferred over reaction 1a in Scheme 1, as rotation of the dithiocarbonyl group, and redistribution of twice as many bonds in reaction 1a *vs* reaction 2a requires overcoming a higher activation energy barrier.

In Scheme 1, Reaction 1a accounts for COS, and reaction 2a for CS₂. Thus, further reactions are needed to explain the evolution of CO₂, CO, EtOH, and H₂O. Also, EtSH as a

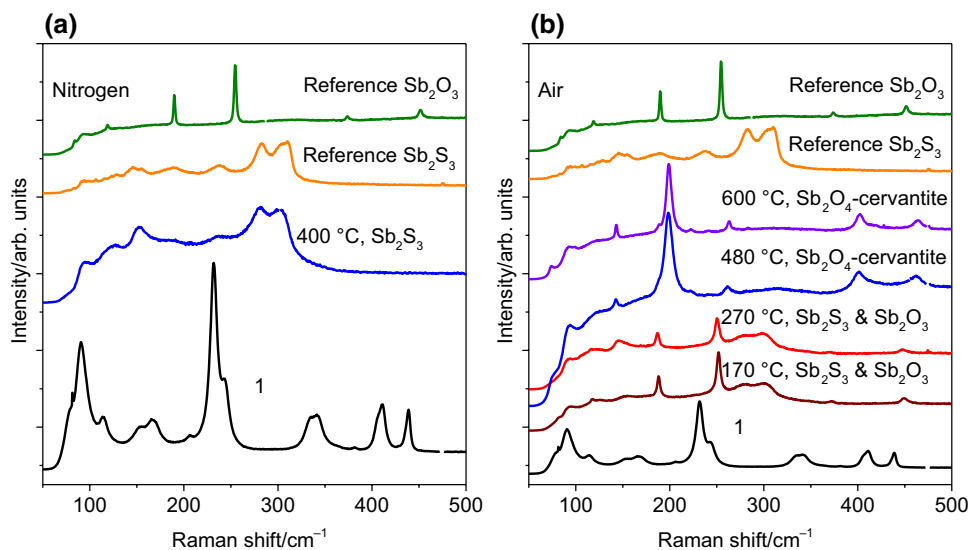


Scheme 1 Proposed decomposition reactions of SbEX occurring in the first decomposition step. $\text{R}_1, \text{R}_2 = \text{EX} / \text{EtO} / \text{EtS} / \text{CSO}_2 / \text{CSO}_2\text{Et} / \text{SH}$

minor gas probably forms in two reaction steps because of steric inhibition of interaction between S and CH_3CH_2^- in the EX ligand, as evinced by NMR and EGA-MS results. Mirroring reaction 1a, CO_2 and EtSH could be produced by reaction 2c in Scheme 1, whereby COS is injected into $\text{Sb}(\text{R}_1)(\text{R}_2)\text{OEt}$ ($\text{R} = \text{EX} / \text{SH} / \text{EtO} / \text{EtS}$), followed by

rearrangement of the COS moiety to yield $\text{Sb}(\text{R}_1)(\text{R}_2)\text{SEt}$ and CO_2 . Reactions like 1b and 2b in Scheme 1, where the metal hydroxide, thiol, alkoxide, or mercaptane reacts as a Lewis base with CS_2 , COS , or CO_2 anhydride as Lewis acid, are known to form carbonates, thiocarbonates, and their alkyl-substituted derivatives [58].

Fig. 5 Raman spectra of **1** and its intermediate decomposition products in laboratory tests in **a** N_2 , flow 60 mL min^{-1} , heating rate 10°min^{-1} after pre-purging to $1 \cdot 10^{-2}$ mbar, heating time 10 min, and in **b** air, where **1** was inserted into a preheated furnace and heated at the specified temperature for 10 min before withdrawal and cooling



Considering the sizeable and rapid mass loss in the first decomposition step, $\text{Sb}(\text{EX})_2\text{OEt}$ could degrade further by decomposition of the remaining EX ligands, followed by evolution of EtOH, *e.g.*, reaction 3 in Scheme 1, while retaining enough Sb-S bonds to form Sb_2S_3 , as confirmed by Raman (Fig. 5b), because no intermediate decomposition products of **1** in inert atmosphere with Sb-O bonding were detected by neither Raman (Fig. 5a) nor XRD (Fig. 6a). By analogy to reaction 3, the remaining EX ligands of $\text{Sb}(\text{EX})_2\text{SEt}$ could decompose, followed by evolution of EtSH (*e.g.*, reaction 4 in Scheme 1).

Judging by EGA-MS evolution intensity (Fig. 3), the evolution of EtSH is an order of magnitude smaller compared to EtOH, meaning the EtS ligand likely undergoes further reactions, acting as a supply of S for Sb_2S_3 , *i.e.*, reaction 5 and reaction 6 in Scheme 1, whereas EtOH evolves directly, *i.e.*, reaction 3 in Scheme 1. Reactions 3–6 in Scheme 1 should proceed, as the interaction between ligands is not sterically inhibited, and because the ligands are small, single-bonded throughout, and therefore able to rotate around the axis of the single coordination bond with Sb. Another possible explanation for the sparse evolution of EtSH could be that reaction 2b is the rate determining step: first, because $\text{Sb}(\text{R}_1)(\text{R}_2)\text{OEt}$ is probably consumed mainly in reaction 3 in Scheme 1 to produce EtOH; second, because the insertion of COS into $\text{Sb}(\text{R}_1)(\text{R}_2)\text{OEt}$ is a gas–liquid reaction limited by the concentration of COS dissolved or dispersed in the liquid mixture.

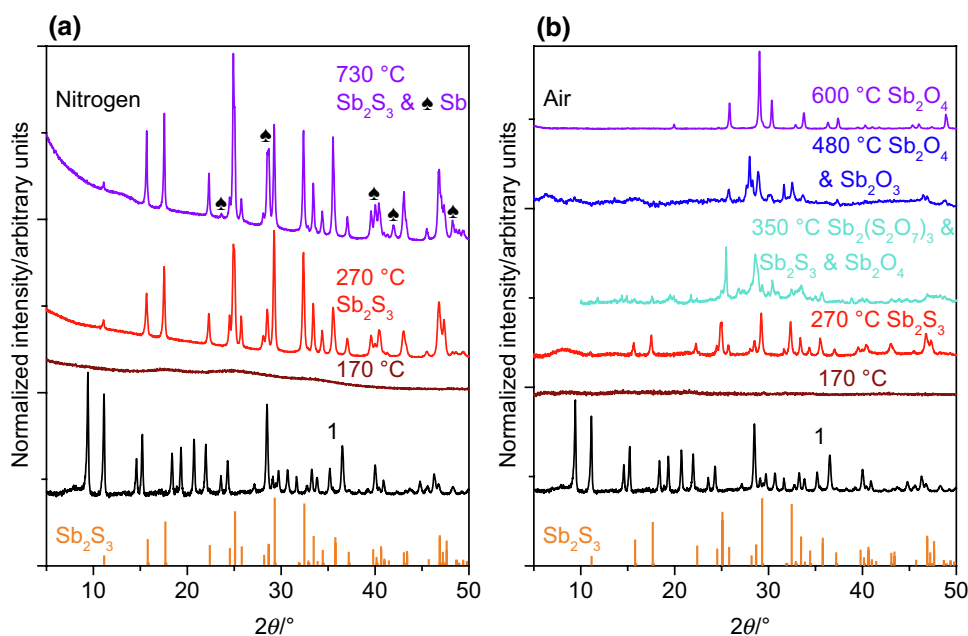
The combined intensity of evolving CO, COS and CO_2 in EGA-MS is similar to the intensity of evolving CS_2 , which could indicate that reaction 2b in Scheme 1 is supplied with COS by reaction 1a or reaction 1c, and with $\text{Sb}(\text{R}_1)(\text{R}_2)\text{OEt}$

by reaction 2a or reaction 1c in Scheme 1. Reaction 1c in Scheme 1 is unlikely to contribute significantly to the thermal decomposition of **1**, because it requires gaseous CO_2 as reactant, which forms in reaction 2c, in turn dependent on COS produced in reaction 1a. Consequently, reaction 1c in Scheme 1 has 6 prerequisite reaction steps before it can occur.

Et_2O and Et_2S are minor byproducts, probably forming via proton transfer between intermediate neighbor ligands and subsequent cleavage from Sb, *e.g.*, reaction 4 and reaction 6 in Scheme 1. SO_2 as a minor gas likely forms in argon by hydrolysis of COS or CS_2 to H_2S and CO_2 or CO, ending with H_2S oxidizing to SO_2 and H_2O [59]. As the quantity of protons is limited in **1** to the ethyl group in the EX ligand above 90 °C, the formation of EtOH, EtSH, and H_2O in argon (and air) requires the formation of an equivalent quantity of ethylene (C_2H_4) via proton transfer to supply the protons. Therefore, the EGA-MS of m/z 28 attributed to CO could be in part attributed to the evolution of C_2H_4 in addition to CO, albeit without definitive proof, as characteristic m/z of C_2H_4 overlap with EtOH and other evolved gases. C_2H_4 could react in air with O_2 to form oxirane ($\text{C}_2\text{H}_4(\text{O})$) or acetaldehyde [4], although neither can be confirmed with EGA-MS due to overlap with m/z of main gases. Water evolves as a product of various decomposition and condensation reactions of intermediate products in the thermal decomposition of SbEX with the atmosphere having no significant effect on its evolution. Finally, CO could evolve from hydrolysis of CS_2 or COS [59], or via incomplete oxidation of EtOH.

The results of this study show that the Chugaev elimination, which is often used to describe xanthate

Fig. 6 XRD patterns of **1** and its intermediate decomposition products in laboratory tests in **a** N_2 , flow 60 mL min^{-1} , heating rate 10°min^{-1} after pre-purging to $1 \cdot 10^{-2}$ mbar, heating time 10 min, and in **b** air, where **1** was inserted into a preheated furnace and heated at the specified temperature for 10 min before withdrawal and cooling



decomposition [35, 37], does not apply for **1** at all, because in it only COS and C₂H₄ are formed – neither the dominant gas in the first decomposition step of **1** (Fig. 3). Clearly, as the Chugaev elimination cannot explain the co-evolution of CS₂, CO, CO₂, H₂O, EtOH, EtSH, Et₂S, and Et₂O in inert and oxidizing atmospheres, the reaction is not valid.

At the end of the first decomposition step at 170 °C in argon, and air, about 3 mass% of the initial mass of organic species is retained in amorphous Sb₂S₃ (Table 3). The solid intermediate prepared at 170 °C in both N₂ and air was amorphous according to XRD, as seen in Fig. 6. However, according to Raman (Fig. 5b), a mixture of Sb₂S₃ and Sb₂O₃ (senarmontite) had formed in air at 170 °C by direct oxidation of Sb₂S₃. The asymmetric shape of the EGA-MS (Fig. 3) curves in addition to the two successive exothermic effects witnessed in DTA (Fig. 2) signifies that either more stable inorganic or organic ligands, *e.g.*, CSO₂²⁻, EtOCOS⁻, EtS⁻, EtO⁻, or a separate dispersed phase has formed inside the amorphous Sb₂S₃ phase, as seen from the FTIR spectra of solid intermediates prepared at 160 °C (Fig. 4). Presumably, the residual organic species are expelled as the gases seen in EGA-MS (Fig. 3), followed by crystallization of purified Sb₂S₃ (Fig. 6), as its nucleation is no longer inhibited. Elucidating the precise composition of this residual impurity in Sb₂S₃, which persists in the solid phase over 100 °C above the first decomposition, warrants further investigation.

The second decomposition step occurred in the range of 170–255 °C in Ar and 170–250 °C in synthetic air, with a mass loss of 2.1% in both cases, evolution of minor amount of CS₂, EtOH, CO, CO₂, COS, H₂O, SO₂, EtSH, Et₂S, Et₂O, and (EX)₂ (Fig. 3), and orthorhombic Sb₂S₃ was the final solid product in inert atmosphere, and a mixture of Sb₂S₃ and cubic Sb₂O₃ in air, as determined by Raman (Fig. 5b). Based on the FTIR analysis of the solid intermediate products (Fig. 4), antimony monothiocarbonate (Sb₂(CSO₂)₃), a trace of antimony ethyl monothiocarbonate (Sb(SOCOCH₂CH₃)₃), and possibly other (thio)carbonyl ligands persist until 240 °C. According to EGA-MS, trace quantities of presumed Sb-SEt, Sb-OEt, or Sb-OSCOEt ligands survive, evolving as EtOH, EtSH, Et₂O, and Et₂S by 250 °C (Fig. 3, Fig. S4). No FTIR bands were observed in any residue prepared at or above 270 °C in either atmosphere (not shown), meaning that all carbonaceous matter had mineralized or evolved by that point, in correlation with the results of EGA-MS (Fig. 3, Fig. S4).

The third decomposition step in synthetic air occurred in the range of 250–495 °C, with a mass loss of 1.0%, accompanied by evolution of SO₂ (Fig. 3), and a mix of Sb₂O₄ and Sb₂O₃ as the final product (Table 3). As seen in Fig. 6b, at 350 °C in air the gray residue contained at least one sulfate of antimony (Sb₂(S₂O₇)₃) in addition to Sb₂S₃, and Sb₂O₄ (cervantite), indicating that in the third decomposition step, any remaining Sb₂S₃ is first oxidized to

a mixture of Sb₂(S_nO_{3n+1})₃ (*n* = 1; 2; 3; 4), *e.g.*, Sb₂(S₂O₇)₃, ICDD 1–070–2198, and Sb₂(SO₄)₂(S₂O₇), 1–083–2537, then to Sb₂O₃, and finally to Sb₂O₄ with vigorous exothermic evolution of SO₂. Therefore, the formation of sulfates above 300 °C in the third decomposition step in air initially caused a slight mass gain that was masked by the net mass loss of 2.6% from the energetic SO₂ evolution. The oxidation rate and oxidation product of Sb₂S₃ at 350–500 °C is strongly dependent on temperature, and particle size [60], which explains the simultaneous detection of antimony compounds in progressive stages of oxidation in the residue.

In the fourth decomposition step in synthetic air in the range of 495–590 °C, the exothermic mass loss at 570 °C coupled with evolution of SO₂ at 575 °C is caused by purification of residual sulfate via transition of senarmontite-Sb₂O₃ into valentinite-Sb₂O₃ at 570 °C (*cf.* 570 °C in [5], 581 °C in [54]), followed by oxidation into Sb₂O₄, as seen by the difference in XRD patterns of residues prepared at 480 °C (senarmontite-Sb₂O₃ & cervantite-Sb₂O₄) and 600 °C (cervantite-Sb₂O₄) in air (Fig. 6b). The intermediate residue prepared in N₂ at 730 °C was composed of Sb₂S₃ and Sb (Fig. 6a). The incongruent evaporation of Sb₂S₃ proceeding above its melting point at 550 °C is complete by 800 °C, which is consistent with results of previous studies [54], where total mass loss of Sb₂S₃ was observed in inert atmosphere.

Similarly to thiourea–metal chloride complexes that we used to deposit SnS, ZnS, CuInS₂, In₂S₃, and Sb₂S₃ thin films by spray pyrolysis for photovoltaic applications [11, 20–22, 61–64], SbEX appears to be an excellent single-source precursor for producing phase pure Sb₂S₃ thin films by spray pyrolysis.

Conclusions

It was shown that, according to FTIR and NMR, **1**, synthesized from KEX and SbCl₃ in molar ratio of Sb/S of 1/3, contains a coordination complex, wherein three -S₂COCH₂CH₃ – ethyl xanthate ligands are coordinated to Sb atom via S atoms. According to elemental analysis and quantitative ¹H NMR, **1** contains approximately 95 mol% of Sb(S₂COCH₂CH₃)₃, and 5 mol% of amorphous Sb₂S₃, as identified by Raman.

The thermal decomposition of **1** consists of three mass loss steps in argon in the temperature range of 90–800 °C, whereas in synthetic air, four mass loss steps occurred in the temperature range of 90–590 °C with mass loss of 100% and 66.8%, respectively. The first and second thermal decomposition steps proceed similarly in argon and synthetic air in the temperature range of 90–170 °C. In argon, amorphous Sb₂S₃ formed as the product of the first decomposition step by 170 °C alongside a minor amount of possibly antimony monothiocarbonate

Sb(CSO₂)₃, Sb(OEt)₃, Sb(SEt)₃ or a mixed ligand compound containing these ligands, identified by EGA-MS and FTIR of intermediate decomposition products. In synthetic air, amorphous senarmontite-Sb₂O₃ formed by 170 °C in addition to the aforementioned compounds, as identified by Raman. In the first decomposition step, CS₂, EtOH, CO, CO₂, COS, H₂O, and SO₂ evolved as main gases. Evolution of minor gases EtSH, Et₂S, Et₂O, and (EX)₂ was also detected.

Chemical reactions occurring in the first decomposition step in the temperature range of 90–170 °C were proposed for the first time for SbEX, describing formation of CS₂, COS, CO₂, EtOH, EtSH, Et₂S, Et₂O, and intermediate decomposition product ligands, *e.g.*, EtS, EtO, and (monothio)carbonyl-based unsubstituted and the respective alkyl-substituted ligands. Furthermore, the results of this study show that the Chugaev elimination reaction is inadequate to describe the thermal decomposition of SbEX.

In the second thermal decomposition step in argon, the solid phase was purified from the remaining ligands, and thereafter Sb₂S₃ crystallized, as confirmed by XRD and Raman. In synthetic air, the solid phase contained amorphous senarmontite-Sb₂O₃, as confirmed by XRD and Raman. The evolved gases in the second thermal decomposition step were the same as in the first step, although evolution of CS₂ and EtOH had diminished considerably. In argon, the third and final thermal decomposition step began at 590 °C, after melting of Sb₂S₃ at 550 °C, and proceeded apace until total mass loss at 800 °C. In air, the third decomposition step began at 250 °C, and ended at 495 °C with the formation of cervantite-Sb₂O₄, proceeding through formation and oxidation of a mixture of antimony sulfates coupled with vigorous evolution of SO₂ (EGA-MS), as shown for the first time for SbEX through solid-phase intermediate decomposition product analysis in this study by XRD and Raman. In the fourth decomposition step in synthetic air, remaining antimony sulfates oxidized into cervantite-Sb₂O₄, as confirmed by XRD of the final product remaining at 600 °C, coupled with evolution of SO₂ according to EGA-MS. Neither evolution of carbonaceous species, nor any presence in the solid state in either atmosphere in intermediate decomposition products prepared at or above 270 °C was detected, indicating that the solid state is free of carbon residues.

Results on the thermal decomposition of *tris*-ethylthiocarbonato-antimony(III) (**1**) in inert and oxidative atmospheres yielded valuable data serving as basis for determining the atmosphere and processing temperatures to be used to deposit phase pure Sb₂S₃ thin films. The fact that SbEX allows to deposit Sb₂S₃ at significantly lower temperatures in comparison to other single-source precursors, and is purified from C containing residues at very low temperatures, makes SbEX a suitable precursor for depositing phase pure Sb₂S₃ thin films by the spray pyrolysis method.

Electronic Supporting Material

The electronic Supplementary File contains the tabulated list of tentative FTIR vibrational assignments from the literature used in this study, the Raman spectrum of **1** in the range of 50–3000 cm⁻¹, and the corresponding tabulated list of tentative Raman vibrational assignments from the literature, the powder XRD pattern of **1**, and the corresponding numeric XRD data, the HMBC plot of **1**, EGA-MS gas evolution curves of additional gaseous species, and peak centers and proposed assignments of all *m/z* channels used in the EGA-MS.

Supplementary Information The online version contains supplementary material available at <https://doi.org/10.1007/s10973-021-10885-1>.

Acknowledgements The authors thank Dr. Valdek Mikli from the Laboratory of Optoelectronic Materials Physics at Tallinn University of Technology for EDX measurements. This study was funded by the Estonian Research Council project PRG627 “Antimony chalcogenide thin films for next-generation semitransparent solar cells applicable in electricity producing windows,” European Regional Development Fund Centre of Excellence project TK141 (TAR16016EK) “Advanced materials and high-technology devices for energy recuperation systems,” and European Regional Development Fund Centre of Excellence project TK134 “Emerging orders in quantum and nanomaterials.”

Author contributions All authors contributed to the study conception and design. Material preparation was performed by J.S. Eensalu. Data collection was performed by J.S. Eensalu, K. Tõnsuaadu and J. Adamson. All authors participated in the data analysis. The first draft of the manuscript was written by J.S. Eensalu and all authors commented on previous versions of the manuscript. All authors read and approved the final and the revised manuscript.

Funding This study was funded by the Estonian Research Council project PRG627 “Antimony chalcogenide thin films for next-generation semitransparent solar cells applicable in electricity producing windows,” European Regional Development Fund Centre of Excellence project TK141 (TAR16016EK) “Advanced materials and high-technology devices for energy recuperation systems,” and European Regional Development Fund Centre of Excellence project TK134 “Emerging orders in quantum and nanomaterials.”

Data availability Data and materials are available upon request from the authors.

Declarations

Conflict of interest The authors declare that they have no conflict of interest.

Open Access This article is licensed under a Creative Commons Attribution 4.0 International License, which permits use, sharing, adaptation, distribution and reproduction in any medium or format, as long as you give appropriate credit to the original author(s) and the source, provide a link to the Creative Commons licence, and indicate if changes were made. The images or other third party material in this article are included in the article's Creative Commons licence, unless indicated otherwise in a credit line to the material. If material is not included in the article's Creative Commons licence and your intended use is not

permitted by statutory regulation or exceeds the permitted use, you will need to obtain permission directly from the copyright holder. To view a copy of this licence, visit <http://creativecommons.org/licenses/by/4.0/>.

References

- Klochko K. Antimony Data Sheet. In: Mineral commodity summaries. U. S. Geological Survey. 2020. Available from: <https://pubs.usgs.gov/periodicals/mcs2020/mcs2020-antimony.pdf>. Accessed 13 May 2020.
- Apodaca LE. Sulfur Data Sheet. In: Mineral commodity summaries. U. S. Geological Survey; 2020. Available from: <https://pubs.usgs.gov/periodicals/mcs2020/mcs2020-sulfur.pdf>. Accessed 13 May 2020.
- Alharbi F, Bass JD, Salhi A, Alyamani A, Kim H-C, Miller RD. Abundant non-toxic materials for thin film solar cells: alternative to conventional materials. *Renew Energy*. 2011;36:2753–8.
- Greenwood NN, Earnshaw A. *Chemistry of the elements*. 2nd ed. Oxford: Butterworth-Heinemann; 1997.
- Thorneycroft WE. Antimony and bismuth. London: Charles Griffin & Co Ltd; 1936.
- Rinkevichius V, Mikalkevichius M. Pyroelectric effect in antimony trisulfide single crystals. *Sov Phys Solid State USSR*. 1967;9:2360.
- Živković Ž, Štrbac N, Živković D, Grujičić D, Boyanov B. Kinetics and mechanism of Sb_2S_3 oxidation process. *Thermochim Acta*. 2002;383:137–43.
- Leijtens T, Bush KA, Prasanna R, McGehee MD. Opportunities and challenges for tandem solar cells using metal halide perovskite semiconductors. *Nat Energy*. 2018;3:828–38.
- Kondrotas R, Chen C, Tang J. Sb_2S_3 Solar cells. *Joule*. 2018;2:857–78.
- Shin HD, Choi S-H. Recent studies of semitransparent solar cells. *Coatings*. 2018;8:329–58.
- Eensalu JS, Katerski A, Kärber E, Weinhardt L, Blum M, Heske C, et al. Semitransparent Sb_2S_3 thin film solar cells by ultrasonic spray pyrolysis for use in solar windows. *Beilstein J Nanotechnol*. 2019;10:2396–409.
- Savado O, Mandal KC. Studies on new chemically deposited photoconducting antimony trisulphide thin films. *Sol Energ Mat Sol Cells*. 1992;26:117–36.
- Zimmermann E, Pfadler T, Kalb J, Dorman JA, Sommer D, Hahn G, et al. Toward high-efficiency solution-processed planar heterojunction Sb_2S_3 solar cells. *Adv Sci (Weinheim, Ger)*. 2015;2:1500059.
- Parize R, Cossuet T, Chaix-Pluchery O, Roussel H, Appert E, Consonni V. In situ analysis of the crystallization process of Sb_2S_3 thin films by Raman scattering and X-ray diffraction. *Mater Des*. 2017;121:1–10.
- Wedemeyer H, Michels J, Chmielowski R, Bourdais S, Muto T, Sugiura M, et al. Nanocrystalline solar cells with an antimony sulfide solid absorber by atomic layer deposition. *Energy Environ Sci*. 2013;6:67–71.
- Kim D-H, Lee S-J, Park MS, Kang J-K, Heo JH, Im SH, et al. Highly reproducible planar Sb_2S_3 -sensitized solar cells based on atomic layer deposition. *Nanoscale*. 2014;6:14549–54.
- Büttner P, Scheler F, Pointer C, Döhler D, Barr MKS, Koroleva A, et al. Adjusting interfacial chemistry and electronic properties of photovoltaics based on a highly pure Sb_2S_3 absorber by atomic layer deposition. *ACS Appl Energy Mater*. 2019;2:8747–56.
- Kaienburg P, Klingebiel B, Kirchartz T. Spin-coated planar Sb_2S_3 hybrid solar cells approaching 5% efficiency. *Beilstein J Nanotechnol*. 2018;9:2114–24.
- Jiang C, Tang R, Wang X, Ju H, Chen G, Chen T. Alkali metals doping for high-performance planar heterojunction Sb_2S_3 solar cells. *Solar RRL*. 2019;3:1800272.
- Kriisa M, Krunks M, Oja Acik I, Kärber E, Mikli V. The effect of tartaric acid in the deposition of Sb_2S_3 films by chemical spray pyrolysis. *Mater Sci Semicond Process*. 2015;40:867–72.
- Kärber E, Katerski A, Oja Acik I, Mere A, Mikli V, Krunks M. Sb_2S_3 grown by ultrasonic spray pyrolysis and its application in a hybrid solar cell. *Beilstein J Nanotechnol*. 2016;7:1662–73.
- Eensalu JS, Katerski A, Kärber E, Oja Acik I, Mere A, Krunks M. Uniform Sb_2S_3 optical coatings by chemical spray method. *Beilstein J Nanotechnol*. 2019;10:198–210.
- Deng H, Yuan S, Yang X, Cai F, Hu C, Qiao K, et al. Efficient and stable $\text{TiO}_2/\text{Sb}_2\text{S}_3$ planar solar cells from absorber crystallization and Se-atmosphere annealing. *Mater Today Energy*. 2017;3:15–23.
- Choi YC, Lee DU, Noh JH, Kim EK, Seok SI. Highly improved Sb_2S_3 sensitized-inorganic–organic heterojunction solar cells and quantification of traps by deep-level transient spectroscopy. *Adv Funct Mater*. 2014;24:3587–92.
- Patil PS. Versatility of chemical spray pyrolysis technique. *Mater Chem Phys*. 1999;59:185–98.
- Krunks M, Leskelä T, Mutikainen I, Niinistö L. A Thermoanalytical study of copper(I) thiocarbamide compounds. *J Therm Anal Calorim*. 1999;56:479–84.
- Otto K, Oja Acik I, Tönsuaadu K, Mere A, Krunks M. Thermoanalytical study of precursors for In_2S_3 thin films deposited by spray pyrolysis. *J Therm Anal Calorim*. 2011;105:615–23.
- Oja Acik I, Otto K, Krunks M, Tönsuaadu K, Mere A. Thermal behaviour of precursors for CuInS_2 thin films deposited by spray pyrolysis. *J Therm Anal Calorim*. 2013;113:1455–65.
- Krunks M, Madarász J, Leskelä T, Mere A, Niinistö L, Pokol G. Study of zinc thiocarbamide chloride, a single-source precursor for zinc sulfide thin films by spray pyrolysis. *J Therm Anal Calorim*. 2003;72:497–506.
- Madarász J, Krunks M, Niinistö L, Pokol G. Evolved gas analysis of dichlorobis(thiourea)zinc(II) by coupled TG-FTIR and TG/DTA-MS techniques. *J Therm Anal Calorim*. 2004;78:679–86.
- Polivtseva S, Oja Acik I, Krunks M, Tönsuaadu K, Mere A. Thermoanalytical study of precursors for tin sulfide thin films deposited by chemical spray pyrolysis. *J Therm Anal Calorim*. 2015;121:177–85.
- Khwaja MA, Cardwell TJ, Magee RJ. Thermal studies on arsenic, antimony and bismuth alkylxanthate complexes. *Anal Chim Acta*. 1973;64:9–17.
- Rodriguez-Castro J, Molloy KC, Liu Y, Lai CS, Dong Z, White TJ, et al. Formation of antimony sulfide powders and thin films from single-source antimony precursors. *J Mater Chem*. 2008;18:5399–405.
- Vreugdenhil AJ, Brienne SHR, Butler IS, Finch JA, Markwell RD. Infrared spectroscopic determination of the gas-phase thermal decomposition products of metal-ethyldithiocarbonate complexes. *Spectrochim Acta, Part A*. 1997;53:2139–51.
- DePuy CH, King RW. Pyrolytic cis eliminations. *Chem Rev*. 1960;60:431–57.
- Chakrabarty T, De AK. Liquid-liquid extraction of arsenic(III), antimony(III) and bismuth(III) with potassium ethyl xanthate. *Fresenius' J Anal Chem*. 1968;242:152–9.
- Zard SZ. On the trail of xanthates: some new chemistry from an old functional group. *Angew Chem, Int Ed Engl*. 1997;36:672–85.
- Talonen P, Sundholm G, Li WH, Floate S, Nichols RJ. A combined in situ infrared spectroscopy and scanning tunnelling

- microscopy study of ethyl xanthate adsorption on Au(111). *Phys Chem Chem Phys*. 1999;1:3661–6.
39. Li J, Liu X, Yao J. The enhanced photovoltaic performance of Sb_2S_3 solar cells by thermal decomposition of antimony ethyl xanthate with thiourea doping. *Energy Technol (Weinheim, Ger)*. 2020;8:1900841.
 40. Garje SS, Jain VK. Chemistry of arsenic, antimony and bismuth compounds derived from xanthate, dithiocarbamate and phosphorus based ligands. *Coord Chem Rev*. 2003;236:35–56.
 41. Ray A, Sathyanarayana DN, Prasad GD, Patel CC. Infrared spectral assignments of methyl and ethyl xanthato complexes of nickel(II). *Spectrochim Acta, Part A*. 1973;29:1579–84.
 42. Buchmaier C, Glänzer M, Torvisco A, Poelt P, Wewerka K, Kunert B, et al. Nickel sulfide thin films and nanocrystals synthesized from nickel xanthate precursors. *J Mater Sci*. 2017;52:10898–914.
 43. Barreca D, Gasparotto A, Maragno C, Seraglia R, Tondello E, Venzo A, et al. Synthesis and characterization of zinc bis(O-isopropylxanthate) as a single-source chemical vapor deposition precursor for ZnS. *Appl Organomet Chem*. 2005;19:1002–9.
 44. Vigneshwaran M, Ohta T, Iikubo S, Kapil G, Ripolles TS, Ogomi Y, et al. Facile synthesis and characterization of sulfur doped low bandgap bismuth based perovskites by soluble precursor route. *Chem Mater*. 2016;28:6436–40.
 45. Bansal N, O'Mahony FTF, Lutz T, Haque SA. Solution processed polymer–inorganic semiconductor solar cells employing Sb_2S_3 as a light harvesting and electron transporting material. *Adv Energy Mater*. 2013;3:986–90.
 46. Wojdyr M. Fityk: a general-purpose peak fitting program. *J Appl Crystallogr*. 2010;43:1126–8.
 47. NIST chemistry webbook. National Institute of Standards and Technology. <https://webbook.nist.gov/chemistry/>. Accessed 28 July 2020.
 48. Juncal LC, Cozzarín MV, Romano RM. Conformational and spectroscopic study of xanthogen ethyl formates, $\text{ROC(S)SC(O)OCH}_2\text{CH}_3$. Isolation of $\text{CH}_3\text{CH}_2\text{OC(O)SH}$. *Spectrochim Acta, Part A*. 2015;139:346–55.
 49. Chandra AP, Puskar L, Simpson DJ, Gerson AR. Copper and xanthate adsorption onto pyrite surfaces: implications for mineral separation through flotation. *Int J Miner Process*. 2012;114–117:16–26.
 50. Woods R, Hope GA. Spectroelectrochemical investigations of the interaction of ethyl xanthate with copper, silver and gold: I. FT-Raman and NMR spectra of the xanthate compounds. *Colloids Surf A*. 1998;137:319–28.
 51. Gottardi G. The crystal structure of xanthates II Antimonious xanthate. *Z Kristallogr Cryst Mater*. 1961;115:451–9.
 52. Hoskins BF, Tiekink ERT, Winter G. The crystal and molecular structure of O-ethylxanthato-bis(quinolin-8-olato)antimony(III) and a redetermination for tris(O-ethylxanthato)antimony(III). *Inorg Chim Acta*. 1985;97:217–22.
 53. Fulmer GR, Miller AJM, Sherden NH, Gottlieb HE, Nudelman A, Stoltz BM, et al. NMR chemical shifts of trace impurities: common laboratory solvents, organics, and gases in deuterated solvents relevant to the organometallic chemist. *Organometallics*. 2010;29:2176–9.
 54. Padilla R, Ramírez G, Ruiz MC. High-temperature volatilization mechanism of stibnite in nitrogen-oxygen atmospheres. *Metall Mater Trans B*. 2010;41:1284–92.
 55. IR spectrum table & chart. Merck KGaA. <https://www.sigmaaldrich.com/technical-documents/articles/biology/ir-spectrum-table.html>. Accessed 10 Jul 2020.
 56. Fisher NG, Dunn JG. Identifying organic foulants on activated carbon from gold processing plants. *Miner Eng*. 2000;13:1581–8.
 57. Fan H-T, Sun W, Jiang B, Wang Q-J, Li D-W, Huang C-C, et al. Adsorption of antimony(III) from aqueous solution by mercapto-functionalized silica-supported organic–inorganic hybrid sorbent: Mechanism insights. *Chem Eng J (Amst, Neth)*. 2016;286:128–38.
 58. Stueber D, Patterson D, Mayne CL, Orendt AM, Grant DM, Parry RW. Carbonates, thiocarbonates, and the corresponding monoalkyl derivatives. 1. Their preparation and isotropic ^{13}C NMR chemical shifts. *Inorg Chem*. 2001;40:1902–11.
 59. Ferm RJ. The chemistry of carbonyl sulfide. *Chem Rev*. 1957;57:621–40.
 60. Padilla R, Aracena A, Ruiz MC. Kinetics of stibnite (Sb_2S_3) oxidation at roasting temperatures. *J Min Metall Sect B*. 2014;50:127–32.
 61. Polivtseva S, Katerski A, Kärber E, Oja Acik I, Mere A, Mikli V, Krunk M. Post-deposition treatment of sprayed SnS films. *Thin Solid Films*. 2017;633:179–84.
 62. Dedova T, Krunk M, Gromyko I, Mikli V, Sildos I, Utt K, et al. Effect of Zn:S molar ratio in solution on the properties of ZnS thin films and the formation of ZnS nanorods by spray pyrolysis. *Phys Status Solidi A*. 2014;211:514–21.
 63. Otto K, Katerski A, Mere A, Volobujeva O, Krunk M. Spray pyrolysis deposition of indium sulphide thin films. *Thin Solid Films*. 2011;519:3055–60.
 64. Krunk M, Mikli V, Bijakina O, Rebane H, Mere A, Varema T, Mellikov E. Composition and structure of CuInS_2 films prepared by spray pyrolysis. *Thin Solid Films*. 2000;361–362:61–4.

Publisher's Note Springer Nature remains neutral with regard to jurisdictional claims in published maps and institutional affiliations.